# PhaCo: an algorithm based on phase closure for the correction of unwrapping errors in SAR interferometry

Angélique Benoit, Béatrice Pinel-Puysségur, Romain Jolivet, Cécile Lasserre

Angélique Benoit, Béatrice Pinel-Puysségur, Romain Jolivet, Cécile Lasserre. PhaCo: an algorithm based on phase closure for the correction of unwrapping errors in SAR interferometry. 2019. hal-02152196v1

HAL Id: hal-02152196
https://hal.science/hal-02152196v1

Preprint submitted on 11 Jun 2019 (v1), last revised 26 Mar 2020 (v2)

# PhaCo: an algorithm based on phase closure for the correction of unwrapping errors in SAR interferometry

Angélique Benoit[1], Béatrice Pinel-Puysségur[2], Romain Jolivet[1] and Cécile Lasserre[3]

[1] Laboratoire de Géologie, Département de Géosciences, Ecole Normale Supérieure, PSL University, UMR CNRS 8538, Paris, France, angelique.benoit@ens.fr.

[2] CEA, DAM, DIF, F-91297 Arpajon, France.

[3] Université de Lyon, UCBL, ENSL, CNRS, LGL-TPE, 69622 Villeurbanne, France.

Accepted: XXX; Received XXX; in original form XXX

Interferometric Synthetic Aperture Radar is commonly used in Earth Sciences to study surface displacements or construct high resolution topographic maps. Recent satellites such as Sentinel-1 constellation allow to derive dense deformation maps with millimetric precision thanks to high revisit frequency. However, InSAR is still limited by interferometric coherence. Interferogram phase noise resulting from a loss of coherence, due to changes in scattering properties between two SAR acquisitions, may lead to unwrapping errors. Unwrapping errors may lead to centimetric errors in time series reconstruction and in the estimation of ground velocity. We present an algorithm based on phase closure of triplets of interferograms to automatically correct unwrapping errors. We describe the algorithm and highlight its performances with two case studies, in Lebanon with Envisat satellite data and in Central Turkey with Sentinel-1 data. The first dataset is particularly affected by unwrapping errors because of long spatial and temporal baseline interferograms and decorrelation due in particular to the presence of vegetation. The second dataset contains unwrapping errors because of temporal changes in the scattering properties of the ground. For these two examples, the algorithm allows the correction of almost all unwrapping errors, without requiring visual inspection or manual deletions, hence preserving regions of interferograms where the phase is polluted by unwrapping errors. We illustrate the efficiency of the algorithm on large datasets (e.g. “big data” problem), such as with Sentinel-1 constellation, where triplets redundancy enhances performances. Finally, we illustrate the influence of our method on time series reconstruction, removing inconsistencies in the derived velocity field.

Radar interferometry – Interferometry – Image processing – Creep and deformation.

## 1 Introduction

Interferometric Synthetic Aperture Radar (InSAR) is a geodetic technique developped in the 70’s for geophysical applications and, originally, to construct topographic maps of the Earth (Graham, 1974; Zebker & Goldstein, 1986), Venus (Rogers & Ingalls, 1970) and the Moon (Zisk, 1972a,b; Margot et al., 2000). In the 90’s, InSAR was then used for the study of surface displacements related to earthquakes (Massonnet et al., 1993; Zebker et al., 1994), inflation of volcanoes (Massonnet et al., 1995) or ice sheet motion (Goldstein et al., 1993). InSAR is based on the acquisition of successive SAR images over the same area and from close positions by a side looking radar onboard a plane or a satellite. The complex conjugate product of two SAR images is called an interferogram. The phase of an interferogram, hereafter called the interferometric phase, corresponds to the relative travel time difference of the electromagnetic wave between two SAR acquisitions. The interferometric phase depends on satellite orbits, topography, spatio-temporal variations in the refractive index of the atmosphere between two acquisitions, ground deformation along the satellite line-of-sight (LOS) and various sources of noise, including Digital Elevation Model and orbits errors and instrumental noise. Measurements of deformation and ground velocity using InSAR have now reached a millimeter accuracy (Simons & Rosen, 2015).

The main limitation of InSAR is interferometric coherence (Rosen et al., 1996). In an interferogram, each pixel phase value corresponds to the phase of the coherent sum of backscattered electromagnetic wave from scatterers on the ground within the pixel. If scattering properties change over time or if the geometry of acquisition is too different between each pass of the satellite, the phase change between two neighbouring pixels may exceed one phase cycle, hence the phase of these pixels might be random in space. Coherence depends on the spatial correlation of phase. A coherence of 1 indicates the phase is constant within the pixel. Over low coherence regions, it is impossible to relate the phase of a pixel with that of the neighbouring pixels, hence it becomes impossible to measure deformation.

Reconstructing continuous signals, including deformation, involves phase unwrapping, which consists in adding the appropriate multiple of $2\pi$ to the interferometric phase. Multiple unwrapping methods have been developed. Branch-cut algorithms consist in identifying consistent or inconsistent paths to integrate the phase signal (Goldstein et al., 1988; Prati et al., 1990; Lin et al., 1994; Herszterg et al., 2018). Least-square techniques, weighted or unweighted, minimize the mean deviation between the estimated (wrapped) and unknown (unwrapped) discrete derivatives of the phase (Ghiglia & Romero, 1994; Flynn, 1997; Costantini, 1998; Chen & Zebker, 2001), sometimes using external data such as GPS to constrain the unwrapping process (Agram & Zebker, 2010). Ultimately, PS methods use the temporal information of multiple interferograms to unwrap the phase in time and space (Pepe & Lanari, 2006; Hooper & Zebker, 2007; Hussain et al., 2016).

Phase unwrapping is based on the hypothesis that the phase of two neighbouring pixels only differs by a fraction of $2\pi$. This hypothesis is only valid in high coherence regions with a moderate fringe rate. When this assumption breaks down, discontinuities in the wrapped phase may lead unwrapping methods to fail, creating artificial offsets of multiples of $2\pi$ in the unwrapped phase. The size of the affected region may vary from a few pixels to a significant fraction of the image. In Earth science applications, almost all interferograms have large regions where phase decorrelates due to changes in scattering properties (e.g. vegetation, humidity, anthropic changes), high topographic gradients or high deformation areas and unwrapping becomes challenging (Simons et al., 2002; Zebker et al., 2007). Unwrapping errors bias estimations of surface deformation by introducing inconsistencies in the interferometric network in case of time series analysis. Unwrapping errors are sometimes manually detected and masked (Jolivet et al., 2012) and methods based on interferometric network misclosure analysis (López-Quiroz et al., 2009) and time series analysis have been proposed (Hussain et al., 2016).

We propose an efficient algorithm, named PhaCo (PHAse unwrapping COrrections), for the correction of unwrapping errors after phase unwrapping, based on the phase closure of interferogram triplets within an interferometric network. A proof of concept of this algorithm has been presented by Pinel-Puysségur et al. (2018) and we describe in details the formulation, implementation and performances of the algorithm in this paper. Phase unwrapping errors detected by the algorithm are automatically corrected iteratively. In the first section, we describe the algorithm. In the second section, we focus on two case studies where decorrelation is high and could be a limiting factor, including data from the Envisat satellite over Lebanon and data from the Sentinel-1 constellation over Turkey. Finally, we discuss performances, limitations and possible improvements of our approach.

## 2 Method

By construction, the sum of three unwrapped interferograms forming a closed loop equals 0 (Fig. 1; Jennison, 1958). For a triplet $T$ of three SAR acquisitions $k$, $l$ and $m$, the triplet phase closure $\Phi_T$ is:

$$\Phi_T = \phi_{kl} + \phi_{lm} - \phi_{km}, \tag{1}$$

where $\phi_{kl}$, $\phi_{lm}$ and $\phi_{km}$ are the unwrapped phases of interferograms computed from acquisitions $k$, $l$ and $m$. By construction, phase closure $\Phi_T$ should be equal to 0. Inconsistencies in phase closure equal to a multiple of $2\pi$ correspond to a phase unwrapping error (De Zan et al., 2015).

Our algorithm detects and corrects such unwrapping errors within a stack of coregistred interferograms formed from SAR images (Fig. 1). First, we identify all triplets in the interferogram network. Second, we compute the phase closure for each triplet following equation 1 and identify groups of pixels with a non-zero phase closure corresponding to regions of unwrapping errors. Third, for each of these incorrectly unwrapped regions, we identify the interferogram incorrectly unwrapped among the three possible ones using the so-called "flux" or "mean closure" methods, described in sections 2.2 and 2.3 respectively. Once we have identified the interferogram incorrectly unwrapped, we correct the unwrapping error. We proceed iteratively through the network of triplets.

## 2.1 Automatic identification of unwrapping errors

For all available triplets, we start by building masks $m_{kl}$, $m_{lm}$ and $m_{km}$ associated to interferograms $I_{kl}$, $I_{lm}$ and $I_{km}$, based on the coherence map. Pixels with a low coherence are masked out. We construct the total mask of the triplet $m_T^{tot}$ as the intersection of masks $m_{kl}$, $m_{lm}$ and $m_{km}$. Then, we compute triplet closure on unwrapped interferograms using equation 1. We distinguish two sources of misclosure in unwrapped interferograms. The first one is unwrapping errors and is specific to unwrapped interferograms. The second one araises from interferogram multilooking prior to unwrapping. Indeed, the multilooking step sums up the contribution of different pixels, sometimes leading to small phase inconsistencies in the wrapped interferograms and thus to non-zero closure (De Zan et al., 2015). We therefore calculate the closure of wrapped interferograms, defined as:

$$\Phi_T^w = (\phi^w_{I_{kl}} + \phi^w_{I_{lm}} - \phi^w_{I_{km}})[2\pi], \tag{2}$$

where $\phi^w_{kl}$, $\phi^w_{lm}$ and $\phi^w_{km}$ are the phase of wrapped interferograms computed from acquisitions $k$, $l$ and $m$. We substract closure of wrapped interferograms $\Phi_T^w$ from closure $\Phi_T$ computed on unwrapped interferograms in order to remove misclosures related to phase consistency loss in multilooking (Eq. 5, Fig. 2). The total triplet closure $\Phi_T^{tot}$ hence writes:

$$\Phi_T^{tot} = (\Phi_T - \Phi_T^w) m_T^{tot}. \tag{3}$$

We then round phase closure modulo $2\pi$. We consider non-zero values as unwrapping errors and group them into regions using structuring elements (Fig. 3b; Verveer, 2003). We consider the largest region with zero misclosure as the reference region. Phase unwrapping errors generally arise in noisy or high fringe rate areas on interferograms. The error spreads from this area, forming a connected region on which phase has been locally correctly unwrapped but is inconsistent with neighbouring regions. We then associate each unwrapping error region to the largest reference region in the vicinity. For each unwrapping error, we determine which interferogram of the triplet has been incorrectly unwrapped using a two-steps detection of unwrapping error.

## 2.2 Step 1: flux method selection

This method identifies which interferogram of a triplet shows an abnormal phase offset, called “flux”, between an unwrapping error and its associated reference region. We first fill up masked pixels within the error zone (Figs 3b and c; Verveer, 2003) and we isolate the inner and outer borders of the error zone using erosion and dilation (Fig. 3d; Matheron, 1967). We discard pixels of the inner border that do not have any neighbour in the outer border, for example when they are on the image border, close to a masked region or far from the reference region. We calculate flux vectors along this boundary by differencing the phase of an inner pixel with the phase of the neighbouring outer pixel (Fig. 3e). We define $p_{flux}$ as the minimum proportion of flux vectors to correct an interferogram (by default 30%). We estimate for each interferogram the proportion of flux vectors equal to a multiple of $2\pi$. If only one interferogram has more than $p_{flux}$ of its flux vectors equal to a multiple of $2\pi$, this one is marked as incorrectly unwrapped and the error is corrected. If two or three interferograms have a proportion greater than $p_{flux}$, we cannot discriminate which interferogram is to be corrected and we try to identify the interferogram using the "mean closure" method.

## 2.3 Step 2: mean closure method selection

If the flux method fails in a triplet, we try to identify the interferogram incorrectly unwrapped by computing the mean closure of the three interferograms for all their triplets. We consider interferogram $I_{kl}$ that belongs to $n$ triplets, $T_1(I_{kl})$ to $T_{N_{I_{kl}}}(I_{kl})$. The mean closure of interferogram $I_{kl}$, noted $\Phi^{mean}_{I_{kl}}$, is defined as the sum of the phase closure $\Phi_n$ on its $N_{I_{kl}}$ triplets, normalized by the number of triplets $N_{I_{kl}}$:

$$\Phi^{mean}_{I_{kl}} = \frac{\sum\limits_{n=1}^{N_{I_{kl}}} \Phi_n}{N_{I_{kl}}} M_{I_{kl}}, \tag{4}$$

where $M_{I_{kl}}$ is the intersection of all masks associated to each triplet. We define $p_{mc}$ as the minimum proportion of pixels equal to a multiple of $2\pi$ to correct an interferogram (by default 50%). We compute the proportion of pixels in the unwrapping error zone that are equal to a multiple of $2\pi$ for the three interferograms of the triplet. If one interferogram has more than $p_{mc}$ pixels equal to a multiple of $2\pi$ in the unwrapping error region, this one is marked as incorrectly unwrapped and the error is corrected. If two interferograms fulfill this condition and if the ratio between the two proportions is greater than $r_{mc}$ (by default 2), the interferogram of highest proportion is corrected. Otherwise, we cannot discriminate which interferogram to correct. As the error may be corrected in another triplet, the algorithm then processes the following triplet.

We have developed an algorithm which detects phase misclosures on a triplet of three interferograms and corrects the interferogram incorrectly unwrapped with a two-steps selection method. We can run the algorithm multiple times until no unwrapping corrections are needed.

## 3 Case studies

We experiment our algorithm on two sets of SAR acquisitions. First, we process the archive of SAR acquisitions from Envisat C-Band satellite over Lebanon. There, unwrapping errors arise because of low phase coherence due to interferograms with long perpendicular baselines and to the presence of vegetation. Second, we process SAR acquisitions from the recent constellation of Sentinel-1 C-Band satellites over Central Turkey. This constellation offers a much shorter revisit time and a larger coverage compared to products from Envisat (revisit time of 6 days, 300 km wide). Manual corrections of unwrapping errors cannot be performed because of the untractable size of the resulting dataset. The two case studies below differ by satellites, processing tools and applications.

### 3.1 Application to Envisat dataset in Lebanon

The Levant fault system is a complex active fault system of 1200 kilometers-long, where large earthquakes of magnitude up to 7.5 happened (e.g. Elias et al., 2007). This major continental fault bounds the Arabian and African plates. We use Envisat satellite archive to measure the interseismic displacement field across this fault system and test our algorithm.

We process data from Envisat ASAR track 78 with NSBAS (Doin et al., 2011), a processing chain based on the Repeat Orbit Interferometry PACkage (ROI_PAC) (Rosen et al., 2004). We coregister SLCs to a master image taking into account local topography (Guillaso et al., 2008). We use DORIS orbits from the European Space Agency (ESA) and SRTM Digital Elevation Model (DEM) (Farr et al., 2007) to compute the orbital and topographic phase contributions. We multilook wrapped interferograms by a factor of 4 in range and 20 in azimuth. We use MuLSAR (Multi-Link Interferograms) in order to increase the signal-to-noise ratio of interferograms (Pinel-Puysségur et al., 2012). We then correct wrapped interferograms from stratified tropospheric delays estimated from ERA-Interim global atmospheric reanalysis data from ECMWF (Doin et al., 2009; Jolivet et al., 2011). We evaluate and compensate DEM errors by estimating the bias induced by perpendicular baselines (Ducret et al., 2014). Finally, we filter interferograms using a Goldstein filter (Goldstein & Werner, 1998), multilook by an additional factor of 4 (16 looks in range, 80 looks in azimuth) and unwrap them using the branch-cut method (Goldstein et al., 1988). Our final dataset is made of 165 unwrapped interferograms.

Our algorithm identifies 282 triplets, among which 186 are corrected. We illustrate automatic corrections with a long temporal baseline interferogram, spanning 4 years, where three corrections are performed (Fig. 4). The first error (number 1 in Fig. 4) is clearly well corrected. The two other errors (number 2 and 3 in Fig. 4) are more challenging due to the effect of filtering on high fringe rate areas. In both cases, a sharp fringe, partially visible on the interferogram before filtering (arrows in Fig. 4d and f), disappears through filtering (arrows in Fig. 4e and g) hence leading to discontinuities in the unwrapped interferograms (red circles in Fig. 4b). After correction, the algorithm restores continuity where a $2\pi$ phase offset was inconsistently introduced by the unwrapping procedure (red circles in Fig. 4c) and discontinuity in high fringe rate areas (arrows in Fig. 4c).

## 3.2 Application to Sentinel-1 dataset in Central Turkey

The North Anatolian Fault is an active right-lateral strike-slip fault which accomodates the rotation of Anatolia with respect to Eurasia. During the 19th century, we observed a westward propagation of large earthquakes ($\sim$M$_W$ 7.0) along this 1200 kilometers-long fault (Stein et al., 1997). The last earthquake is the Izmit event M$_W$ 7.5 in 1999, east of the Sea of Marmara (e.g. Reilinger et al., 2000).

We process data from Sentinel-1 track 87 with the InSAR Scientific Computing Environment (ISCE) software (Gurrola et al., 2010). We define the acquisition of July, 9th 2017 as the master Single Look Complex (SLC) and coregister slave SLCs to this master image. Coregistration is enhanced using the spectral diversity of burst overlaps refined within the network of interferograms (Fattahi et al., 2017). We generate interferograms, accounting for digital elevation model (SRTM Version 3.0; Farr et al., 2007) and orbital contributions, and merge tiles for each of them using bursts and swaths overlaps. We multilook merged interferograms with factors of respectively 81 and 27 in azimuth and range directions for a final pixel size of 540 x 420 meters, in range and azimuth respectively. We correct the phase from tropospheric signals using ERA-5, the latest global atmospheric reanalysis from ECMWF (Hersbach & Dee, 2016). Finally, we filter (Goldstein & Werner, 1998) and unwrap interferograms using the branch-cut method (Goldstein et al., 1988). We manually remove from the dataset interferograms that cannot be unwrapped because of large, low coherence regions. Our final dataset is made of 686 coregistered and unwrapped interferograms.

Our algorithm identifies 5645 triplets, among which 986 triplets are finally corrected (Fig. 5a). We calculate the percentage of corrected pixels per interferogram by summing the number of pixels detected as unwrapping errors and corrected by the algorithm in all triplets of the interferogram. We see that most of the interferograms are totally corrected from unwrapping errors during a first pass of the algorithm (Fig. 5b). We illustrate automatic corrections with two examples of corrected interferograms, one with a large unwrapping error of 10388 pixels (4% of the interferogram, Fig. 5c) and another with two unwrapping errors localized in different places (Fig. 5d). In both cases, 99% of the unwrapping error is automatically detected and corrected by the algorithm. Uncorrected pixels are located in the masked region of the triplet. The second example shows that the algorithm can perform multiple corrections in a single interferogram (Fig. 5d). In this case, it detects two unwrapping errors in the same interferogram and corrects them in the same triplet.

# 4 Discussion

## 4.1 Performances of the algorithm and time series analysis

One potential application of SAR interferometry is to perform time series analysis and estimate ground velocity over a given region from a stack of interferograms. We illustrate the effect of automatic corrections of unwrapping errors on the estimation of ground velocity and the associated error decrease on ground surface deformation measurement.

We perform two time series analysis on the Sentinel-1 dataset (Section 3.2): the first one is applied to the original stack of interferograms not corrected from unwrapping errors, the second one is applied to the interferograms corrected by the proposed approach. We invert the phase temporal evolution for both datasets identically using the small baseline NSBAS approach (Doin et al., 2011) implemented in the Generic InSAR Analysis Toolbox (GIAnT) (Agram et al., 2012). In this method, we consider each pixel independently to recover the time phase change (López-Quiroz et al., 2009; Doin et al., 2011; Jolivet et al., 2012).

For each time series analysis, we first remove interferograms that have less than 35% unwrapped pixels, hence reducing the dataset to 627 interferograms. We then multilook interferograms by a factor of 2 and spatially reference them by choosing a region where the phase is set to be equal in all interferograms. We correct orbital biases in interferograms by estimating a linear ramp. Terms of the ramp are refined accounting for the interferometric network (Lin et al., 2010; Jolivet et al., 2012). We then perform a least squares inversion of phase delays of each pixel to solve for the total phase delay of each date relative to the first date and for a parametric evolution of phase change across the whole acquisition period. The parametric evolution of surface deformation is a combination of a linear term and a seasonal-annual function.

We obtain two velocity maps over Central Turkey (Fig. 6a and b). If we do not correct interferograms from unwrapping errors before the inversion, surface velocity is strongly affected by unwrapping errors (Fig. 6a, b, d and e). In particular, several suspicious discontinuities visible on the first velocity map (Fig 6a and 6d) are not detected on the second one (Fig 6b and 6e). Errors in velocity can reach up to 4 mm/yr in large regions (Fig. 6c), corresponding in our case to 20% of the expected tectonic displacement in the area. We can also identify small differences of 1 mm/yr (Fig. 6c and f), due to a difference in referencing between the two velocity maps. If we choose a reference region within an unwrapping error, the inversion will differ hence the resulting velocity maps will be different. Unwrapping errors have also a large contribution on Root Mean Square (RMS) error maps. The RMS is defined as:

$$\Phi_{RMS} = \frac{1}{N} \left[ \sum_{N} \left( \phi_{ij} - \sum_{k=i}^{j-1} m_k \right)^2 \right]^{1/2}, \tag{5}$$

where $\phi_{ij}$ is the measured phase between acquisitions $i$ and $j$ and $\sum_{k=i}^{j-1} m_k$ is the reconstructed phase between the same acquisitions (Fig. 7; Cavalié et al., 2007). If we do not correct interferograms from unwrapping errors before the inversion, RMS errors reaches 12 mm (Fig. 7a), compared to few millimeters if unwrapping errors are corrected with the proposed approach (Fig. 7c). On average, the RMS is of 1.61 mm and 0.98 mm, respectively. In the case where unwrapping errors are not corrected, deviation in RMS is much larger than when errors are corrected, with extreme values of 8 to 14 mm (Fig. 7b). When we perform automatic corrections of unwrapping errors, we remove extreme values and we reduce RMS to values close to 1 mm (Fig. 7d). We expect this result, as the algorithm is designed to reduce misclosure of the network. As pixels with a high RMS value after time series analysis cannot be trusted for further interpretation, our approach allows to extend the area over which we can interpret the LOS displacement signal. Therefore, correcting unwrapping errors allows to expand the zone over which we confidently measure ground velocity, in the present case by 20% with a RMS threshold of 3 mm.

To conclude, as unwrapping errors can lead to centimetric errors in the measured velocity, the proposed approach is very helpful as it significantly decreases the RMS error associated to the time series inversion.

## 4.2 Limits and development

We have illustrated on two case studies the efficiency of our algorithm to automatically detect and correct unwrapping errors on a network of interferograms. As the algorithm is based on triplet information, the more interferograms are constructed, the largest the network of triplets is built, hence the higher the probability to correct recurrent unwrapping errors. The algorithm is particularly powerful for large datasets such as from Sentinel-1, where the revisit time is 6 days hence allowing to construct large networks.

Despite the efficiency of our algorithm, there are some limitations. Processing time is one of the main constraint and depends on the size of the dataset. For example, the algorithm takes about six hours to process the Turkey dataset, which corresponds to 5645 triplets, using 24 threads on a single CPU machine. One way to increase the speed of processing is to take more benefits from triplets information considering the first iteration. The goal is to determine which interferograms to correct first so that it helps for the correction of other interferograms, hence reducing processing time. For instance, triplets with small-baseline interferograms should be corrected in priority as they are supposed to be less affected by decorrelation and therefore less affected by unwrapping errors. Long-baseline interferograms should be corrected afterwards, using triplets where small-baseline interferograms have been corrected. Another improvement would be to parallelize some of the steps of the algorithm, for instance to deal with independent triplets in parallel.

# 5 Conclusion

We developed an algorithm called PhaCo, which uses phase closure of triplets of interferograms to correct unwrapping errors left by the phase unwrapping process. We assessed its efficiency on two datasets in Lebanon and Turkey, respectively with Envisat and Sentinel-1 satellites.

The algorithm follows phase unwrapping techniques such as branch-cut or least-square methods. It helps to preserve regions of interferograms where the phase is polluted by unwrapping errors, without requiring visual interferogram inspection or manual deletions of unwrapping errors.

As the contribution of unwrapping errors to velocity maps may reach up to 1 cm/yr and as they lead to RMS errors up to 1 cm, it is critical to correct these errors for interseismic strain measurements in active tectonic environments, where deformation rates are typically on the order of a millimeter per year. Our automatic method, designed for dense networks of interferograms, fits well into existing lines of research, where we increasingly face “big data” related challenges, which must be converted from a highway to hell to a stairway to heaven.

# 6 Acknowledgments

This project received fundings from the European Research Council (ERC) under the European Union's Horizon 2020 research and innovation program (Geo-4D project, grant agreement 758210). We use the Sentinel-1 and Envisat products, respectively provided by the Plateforme d'Exploitation des Produits Sentinel (PEPS) for Turkey and ESA through Cat1 proposal and EOLi-SA platform for Lebanon. We process acquisitions using the ISCE system developped at JPL/Caltech (Turkey) and NSBAS chain based on ROI_PAC as well (Lebanon). This work was partially supported by The Laboratoire de Recherche Commun Yves Rocard. Data analysis on Lebanon was supported by CNES through the TOSCA program. The code of our open-source algorithm is available on Github.

# References

Agram, P., Jolivet, R., & Simons, M., 2012. Generic InSAR Analysis Toolbox (GIAnT) - User Guide, *http://earthdef.caltech.edu*.

Agram, P. S. & Zebker, H., 2010. Edgelist phase unwrapping algorithm for time series InSAR analysis, *J. Opt. Soc. Am. A*, **27**(3).

Cavalié, O., Doin, M.-P., Lasserre, C., & Briole, P., 2007. Ground motion measurement in the Lake Mead area, Nevada, by differential synthetic aperture radar interferometry time series analysis: Probing the lithosphere rheological structure, *J. Geophys. Res.*, **112**(B3).

Chen, C. W. & Zebker, H. A., 2001. Two-dimensional phase unwrapping with use of statistical models for cost functions in nonlinear optimization, *J. Opt. Soc. Am. A*, **18**(2), 338–351.

Costantini, M., 1998. A novel phase unwrapping method based on network programming, *IEEE Trans. Geosci. Remote Sens.*, **36**(3), 813–821.

De Zan, F., Zonno, M., & Lopez-Dekker, P., 2015. Phase Inconsistencies and Multiple Scattering in SAR Interferometry, *IEEE Trans. Geosci. Remote Sens.*, **53**(12), 6608–6616.

Doin, M.-P., Lasserre, C., Peltzer, G., Cavalié, O., & Doubre, C., 2009. Corrections of stratified tropospheric delays in SAR interferometry: Validation with global atmospheric models, *J. Appl. Geophys.*, **69**(1), 35–50.

Doin, M.-P., Lodge, F., Guillaso, S., Jolivet, R., Lasserre, C., Ducret, G., Grandin, R., Pathier, E., & Pinel, V., 2011. Presentation of the small baseline NSBAS processing chain on a case example: the Etna deformation monitoring from 2003 to 2010 using Envisat data, *Proc. ESA 'Fringe 2011 Work. Frascati, Italy, (19-23 Sept. 2011)*, pp. 19–23.

Ducret, G., Doin, M.-P., Grandin, R., Lasserre, C., & Guillaso, S., 2014. DEM Corrections Before Unwrapping in a Small Baseline Strategy for InSAR Time Series Analysis, *IEEE Geosci. Remote Sens. Lett.*, **11**(3), 696–700.

Elias, A., Tapponnier, P., Singh, S. C., King, G. C., Briais, A., Daëron, M., Carton, H., Sursock, A., Jacques, E., Jomaa, R., & Klinger, Y., 2007. Active thrusting offshore Mount Lebanon: Source of the tsunamigenic A.D. 551 Beirut-Tripoli earthquake, *Geology*, **35**(8).

Farr, T. G., Rosen, P. A., Caro, E., Crippen, R., Duren, R., Hensley, S., Kobrick, M., Paller, M., Rodriguez, E., Roth, L., Seal, D., Shaffer, S., Shimada, J., Umland, J., Werner, M., Oskin, M., Burbank, D., & Alsdorf, D., 2007. The Shuttle Radar Topography Mission, *Rev. Geophys.*, **45**(2).

Fattahi, H., Agram, P., & Simons, M., 2017. A Network-Based Enhanced Spectral Diversity Approach for TOPS Time-Series Analysis, *IEEE Trans. Geosci. Remote Sens.*, **55**(2), 777–786.

Flynn, T. J., 1997. Two-dimensional phase unwrapping with minimum weighted discontinuity, *J. Opt. Soc. Am. A*, **14**(10).

Ghiglia, D. C. & Romero, L. A., 1994. Robust two-dimensional weighted and unweighted phase unwrapping that uses fast transforms and iterative methods, *J. Opt. Soc. Am. A*, **11**(1).

Goldstein, R. M. & Werner, C. L., 1998. Radar interferogram filtering for geophysical applications, *Geophys. Res. Lett.*, **25**(21), 4035–4038.

Goldstein, R. M., Zebker, H. A., & Werner, C. L., 1988. Satellite radar interferometry: Two-dimensional phase unwrapping, *Radio Sci.*, **23**(4), 713–720.

Goldstein, R. M., Engelhardt, H., Kamb, B., & Frolich, R. M., 1993. Satellite Radar Interferometry for Monitoring Ice Sheet Motion: Application to an Antarctic Ice Stream, *Science (80-. ).*, **262**(5139), 1525–1530.

Graham, L., 1974. Synthetic interferometer radar for topographic mapping, *Proc. IEEE*, **62**(6), 763–768.

Guillaso, S., Lasserre, C., Doin, M.-P., Cavalie, O., Sun, J., & Pelzer, G., 2008. InSAR measurement of interseismic strain in areas of low coherence: example across the Haiyuan fault (Gansu, China) using a local InSAR adaptive range filter, *EGU*, **10**.

Gurrola, E., Rosen, P. A., Sacco, G. F., Seliga, W., Zebker, H., Simons, M., & Sandwell, D., 2010. InSAR Scientific Computing Environment, *2010 Am. Geophys. Union Meet.*.

Hersbach, H. & Dee, D., 2016. ERA5 reanalysis is in production, *ECMWF Newsl.*, **147**.

Herszterg, I., Poggi, M., & Vidal, T., 2018. 2D-Phase Unwrapping via Balanced Spanning Forests, (1995).

Hooper, A. & Zebker, H. A., 2007. Phase unwrapping in three dimensions with application to InSAR time series, *J. Opt. Soc. Am. A*, **24**(9).

Hussain, E., Hooper, A., Wright, T. J., Walters, R. J., & Bekaert, D. P. S., 2016. Interseismic strain accumulation across the central North Anatolian Fault from iteratively unwrapped InSAR measurements, *J. Geophys. Res. Solid Earth*, **121**(12), 9000–9019.

Jennison, R. C., 1958. A Phase Sensitive Interferometer Technique for the Measurement of the Fourier Transforms of Spatial Brightness Distributions of Small Angular Extent, *Mon. Not. R. Astron. Soc.*, **118**(3), 276–284.

Jolivet, R., Grandin, R., Lasserre, C., Doin, M.-P., & Peltzer, G., 2011. Systematic InSAR tropospheric phase delay corrections from global meteorological reanalysis data, *Geophys. Res. Lett.*, **38**(17).

Jolivet, R., Lasserre, C., Doin, M.-P., Guillaso, S., Peltzer, G., Dailu, R., Sun, J., Shen, Z.-K., & Xu, X., 2012. Shallow creep on the Haiyuan Fault (Gansu, China) revealed by SAR Interferometry, *J. Geophys. Res. Solid Earth*, **117**(B6).

Lin, Q., Vesecky, J. F., & Zebker, H. A., 1994. Phase unwrapping through fringe-line detection in synthetic aperture radar interferometry, *Appl. Opt.*, **33**(2).

Lin, Y.-n. N., Simons, M., Hetland, E. A., Muse, P., & DiCaprio, C., 2010. A multiscale approach to estimating topographically correlated propagation delays in radar interferograms, *Geochem., Geophys. Geosys.*, **11**(9).

López-Quiroz, P., Doin, M.-p., Tupin, F., Briole, P., & Nicolas, J.-m., 2009. Time series analysis of Mexico City subsidence constrained by radar interferometry, *J. Appl. Geophys.*, **69**(1), 1–15.

Margot, J.-L., Campbell, D., Jurgens, R., & Slade, M., 2000. Digital elevation models of the Moon from Earth-based radar interferometry, *IEEE Trans. Geosci. Remote Sens.*, **38**(2), 1122–1133.

Massonnet, D., Rossi, M., Carmona, C., Adragna, F., Peltzer, G., Feigl, K., & Rabaute, T., 1993. The displacement field of the Landers earthquake mapped by radar interferometry, *Nature*, **364**(6433), 138–142.

Massonnet, D., Briole, P., & Arnaud, A., 1995. Deflation of Mount Etna monitored by spaceborne radar interferometry, *Nature*, **375**(6532), 567–570.

Matheron, G., 1967. *Elements pour une theorie des milieux poreux*, Paris, masson edn.

Pepe, A. & Lanari, R., 2006. On the Extension of the Minimum Cost Flow Algorithm for Phase Unwrapping of Multitemporal Differential SAR Interferograms, *IEEE Trans. Geosci. Remote Sens.*, **44**(9), 2374–2383.

Pinel-Puysségur, B., Michel, R., & Avouac, J.-P., 2012. Multi-Link InSAR Time Series: Enhancement of a Wrapped Interferometric Database, *IEEE J. Sel. Top. Appl. Earth Obs. Remote Sens.*, **5**(3), 784–794.

Pinel-Puysségur, B., Lasserre, C., Benoit, A., Jolivet, R., Doin, M.-p., & Champenois, J., 2018. A Simple Phase Unwrapping Errors Correction Algorithm Based on Phase Closure Analysis, in *IGARSS 2018 - 2018 IEEE Int. Geosci. Remote Sens. Symp.*, vol. 1, pp. 2212–2215, IEEE.

Prati, C., Giani, M., & Leuratti, N., 1990. SAR Interferometry: A 2-D Phase Unwrapping Technique Based On Phase And Absolute Values Informations, in *10th Annu. Int. Symp. Geosci. Remote Sens.*, pp. 2043–2046, IEEE.

Reilinger, R. E., Ergintav, S., Bürgmann, R., McClusky, S., Lenk, O., Barka, A., Gurkan, O., Hearn, L., Feigl, K. L., Cakmak, R., Aktug, B., Ozener, H., & Töksoz, M. N., 2000. Coseismic and Postseismic Fault Slip for the 17 August 1999, M = 7.5, Izmit, Turkey Earthquake, *Science (80-. ).*, **289**(5484), 1519–1524.

Rogers, A. E. E. & Ingalls, R. P., 1970. Radar Mapping of Venus With Interferometric Resolution of the Range-Doppler Ambiguity, *Radio Sci.*, **5**(2), 425–433.

Rosen, P. A., Hensley, S., Zebker, H. A., Webb, F. H., & Fielding, E. J., 1996. Surface deformation and coherence measurements of Kilauea Volcano, Hawaii, from SIR-C radar interferometry, *J. Geophys. Res.*, **101**(E10).

Rosen, P. A., Hensley, S., Peltzer, G., & Simons, M., 2004. Updated repeat orbit interferometry package released, *Eos, Trans. Am. Geophys. Union*, **85**(5).

Simons, M. & Rosen, P., 2015. Interferometric Synthetic Aperture Radar Geodesy, in *Treatise Geophys.*, vol. 3, pp. 339–385, Elsevier.

Simons, M., Fialko, Y., & Riviera, L., 2002. Coseismic Deformation from the 1999 Mw 7.1 Hector Mine, California, Earthquake as Inferred from InSAR and GPS Observations, *Bull. Seismol. Soc. Am.*, **92**(4), 1390–1402.

Stein, R. S., Barka, A. A., & Dieterich, J. H., 1997. Progressive failure on the North Anatolian fault since 1939 by earthquake stress triggering, *Geophys. J. Int.*, **128**(3), 594–604.

Verveer, P., 2003. GitHub repository, SciPy library.

Zebker, H., Shankar, P., & Hooper, A., 2007. InSAR Remote Sensing Over Decorrelating Terrains: Persistent Scattering Methods, in *2007 IEEE Radar Conf.*, pp. 717–722, IEEE.

Zebker, H. A. & Goldstein, R. M., 1986. Topographic mapping from interferometric synthetic aperture radar observations, *J. Geophys. Res.*, **91**(B5), 4993–4999.

Zebker, H. A., Rosen, P. A., Goldstein, R. M., Gabriel, A., & Werner, C. L., 1994. On the derivation of coseismic displacement fields using differential radar interferometry: The Landers earthquake, *J. Geophys. Res. Solid Earth*, **99**(B10).

Zisk, S. H., 1972a. Lunar Topography: First Radar-Interferometer Measurements of the Alphonsus-Ptolemaeus-Arzachel Region, *Science (80-. ).*, **178**(4064), 977–980.

Zisk, S. H., 1972b. A new, earth-based radar technique for the measurement of lunar topography, *Moon*, **4**(3-4), 296–306.

Table 1: Default values for the algorithm thresholds

| Name | Value (default) |
|---|---|
| $minSize$ | 200 |
| $p_{flux}$ | 0.30 |
| $p_{mc}$ | 0.5 |
| $r_{mc}$ | 2 |

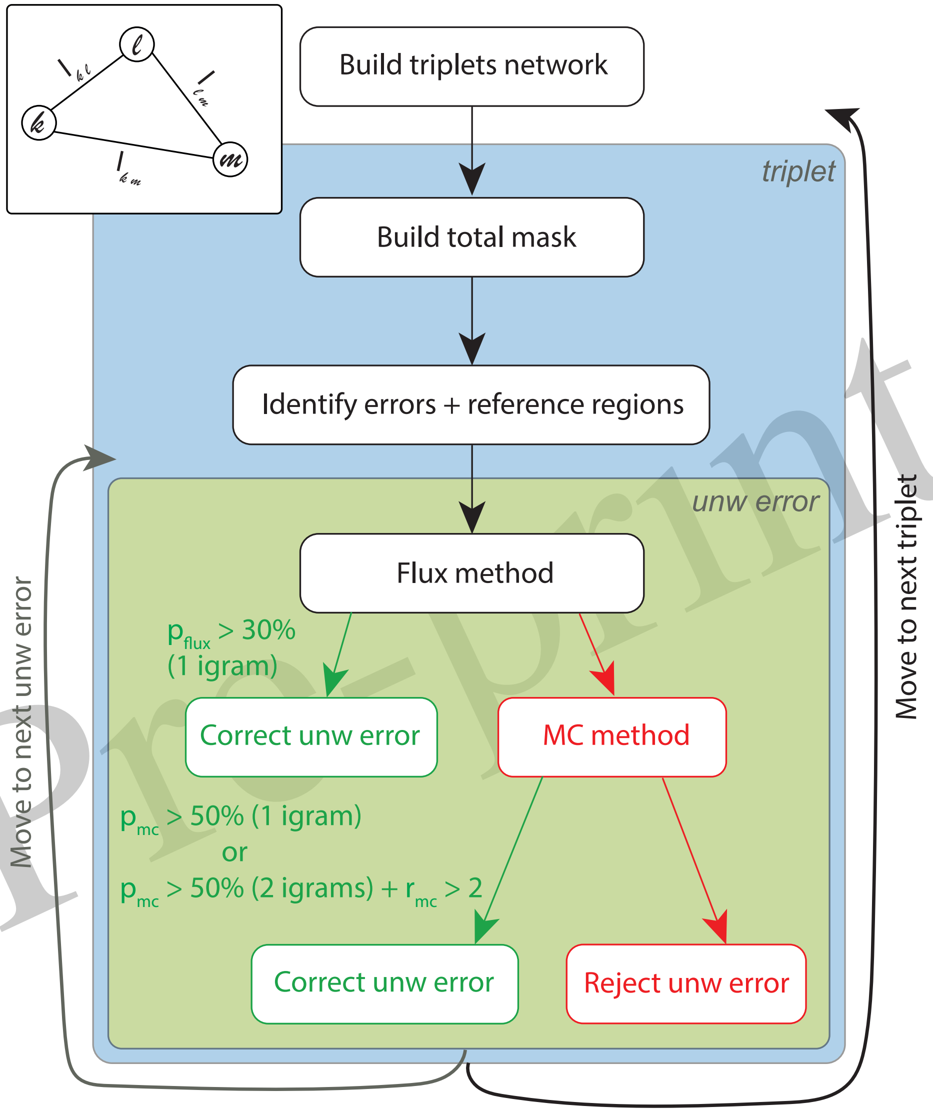

Figure 1: Algorithm implementation. First, we build the network of triplets. We process then each triplet. We identify unwrapping errors and reference regions using triplet phase closure. We correct each unwrapping error using a two-steps detection, with the flux method or with the mean closure method, in case the flux method cannot determine which interferogram to correct.

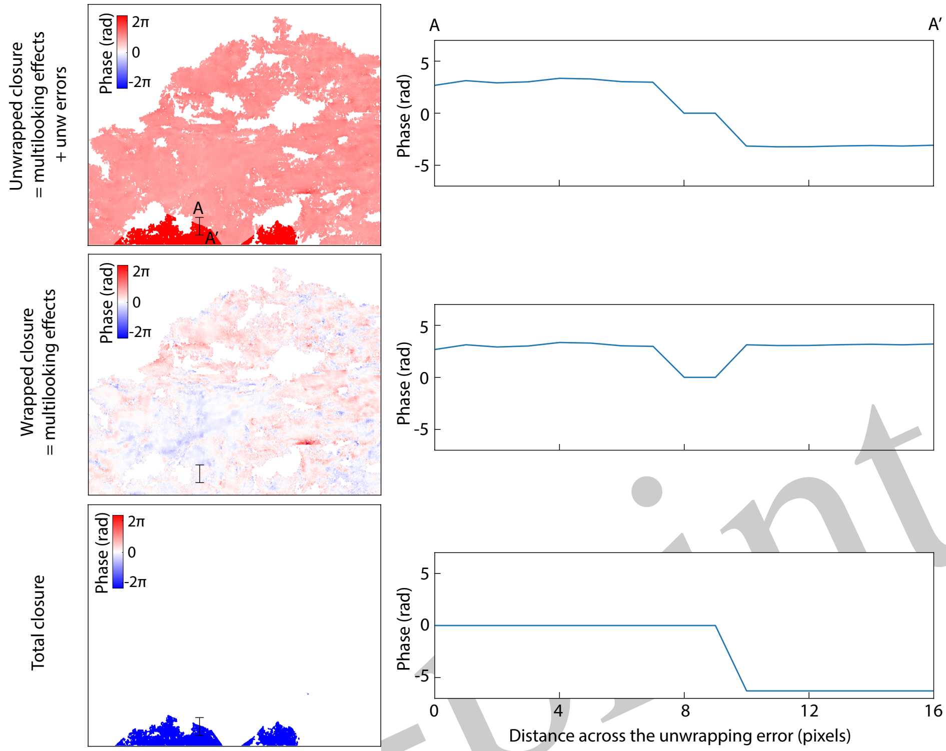

Figure 2: Closure maps (left) and profiles across an unwrapping error (right). Top) Closure from unwrapped interferograms. Center) Closure from wrapped interferograms. Non zero closure is due to multilooking. Bottom) Total closure computed by removing misclosures due to multilooking effects.

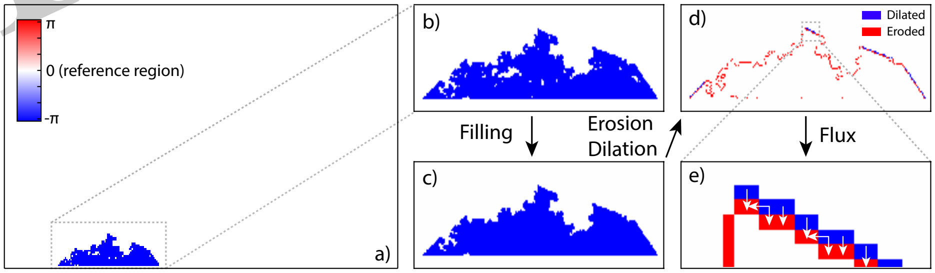

Figure 3: Steps to identify and correct an unwrapping error by the so-called flux method. a) Total phase closure of the triplet. b-c) Masked pixels within the unwrapping error zone are filled by erosion and dilation tool. d) Erosion and dilation of the unwrapping error zone to identify inner (red) and outer (blue) border. e) Computation of flux vectors between outer and inner pixels of the unwrapping error.

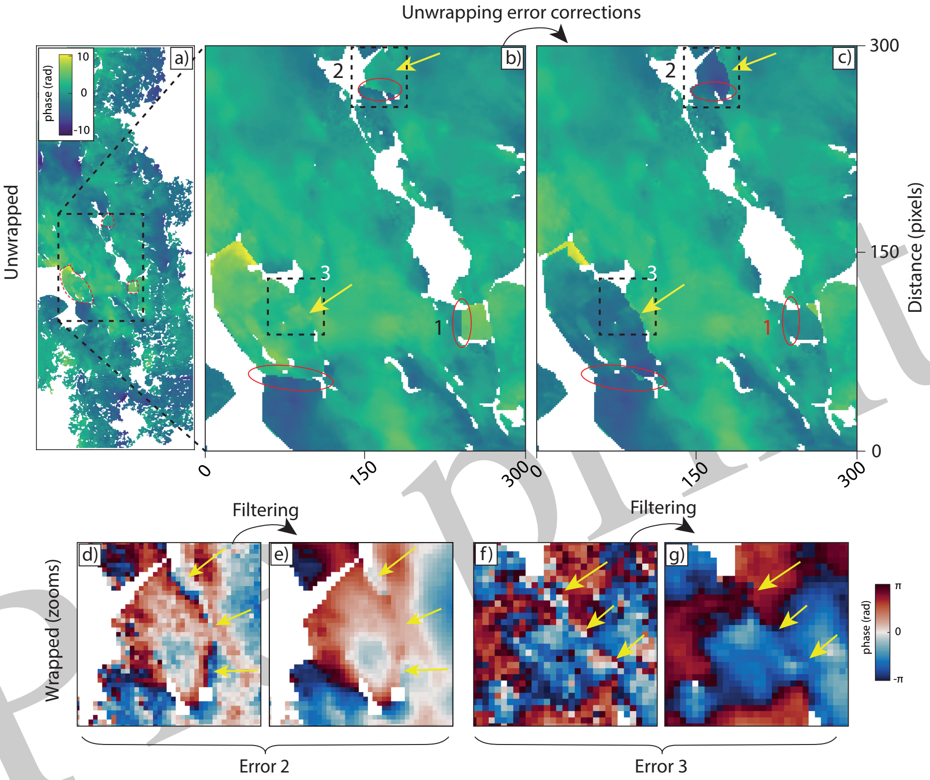

Figure 4: Results for Envisat dataset in Lebanon. a) Example of an interferogram spanning 20040801 - 20080706 which contains unwrapping errors (red circles). b) and c) Zooms of not corrected and corrected unwrapped interferograms. Error 1 is well corrected by the algorithm. Errors 2 and 3 are challenging areas, where the high fringe gradient, visible on wrapped interferograms, disappears by filtering before unwrapping (arrows in b). The algorithm restores the correct positions of offsets (arrows in c). d), e), f) and g) Zooms of unwrapping errors 2 and 3 on wrapped interferograms, before and after filtering. Filtering erases fringes in high fringe rate regions (arrows).

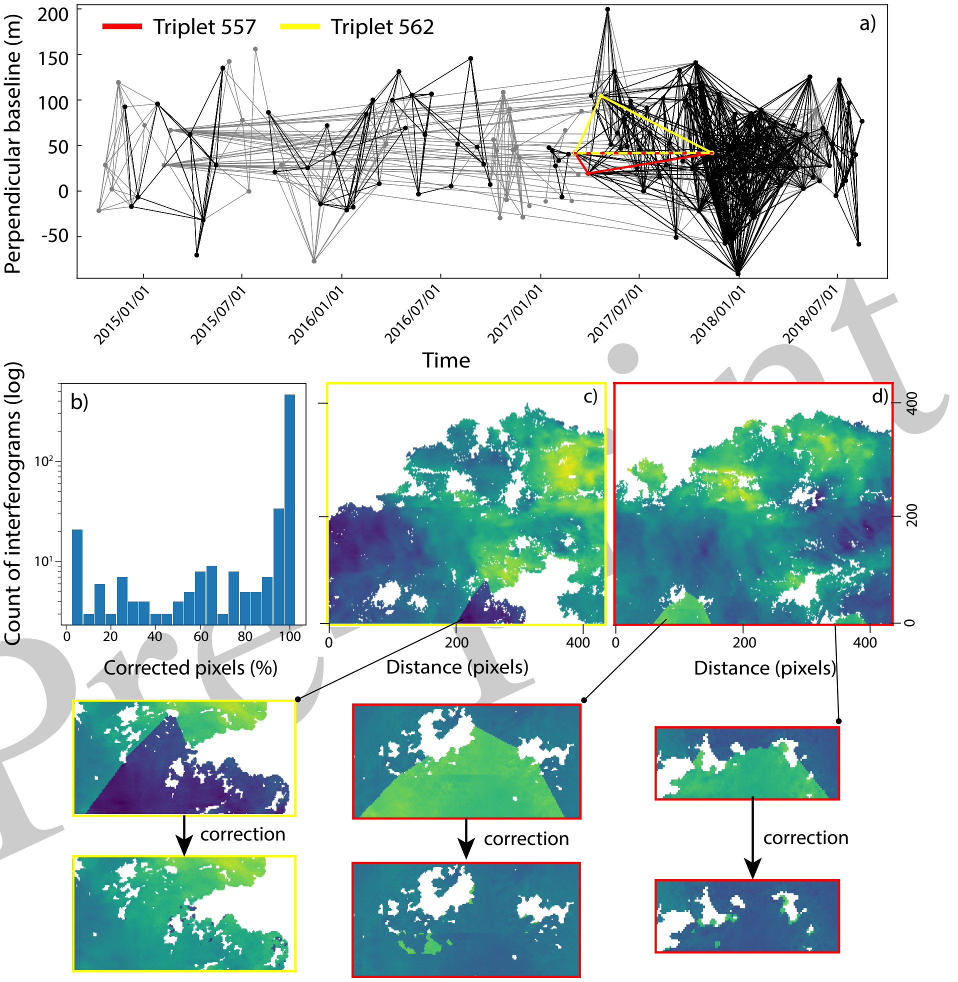

Figure 5: Results for Sentinel-1 dataset in Turkey. a) Perpendicular baseline plot with corrected triplets in black. Dots are SAR acquisitions and lines are interferograms. b) Histogram of the number of interferograms corrected as a function of percentage of corrected pixels. c) and d) Examples of corrections spanning 20170422 - 20171112 and 20170305 - 20171112, respectively.

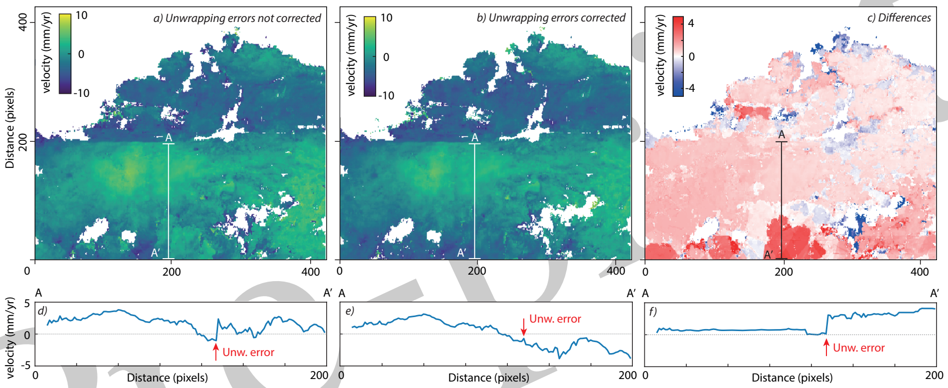

Figure 6: Influence of unwrapping error corrections on time series analysis. a) Velocity map calculated from a stack of interferograms not corrected from unwrapping errors and b) from a stack of interferograms corrected from unwrapping errors. c) Differences between a and b. d) e) and f) Profiles across a, b and c, respectively.

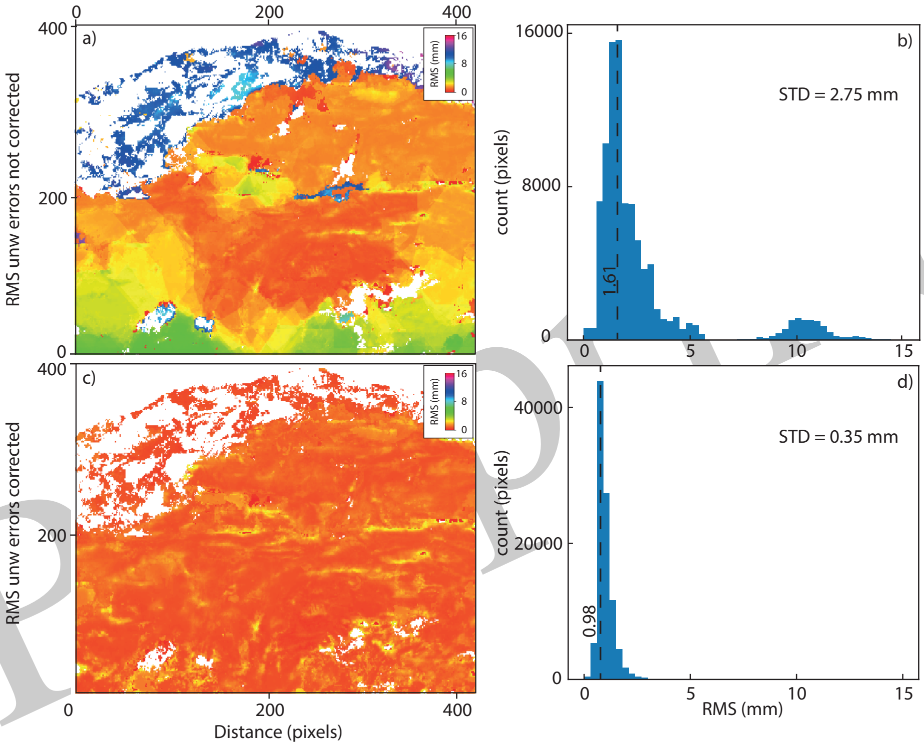

Figure 7: Influence of unwrapping errors on root mean square (RMS) maps. a) and c) RMS maps where unwrapping errors are not corrected and corrected, respectively. Unwrapping errors have a large contribution on the estimation of RMS. b) and d) Histograms of RMS maps a and c, respectively.